optica

Compressive ultrafast pulse measurement via time-domain single-pixel imaging

JIAPENG ZHAO,[1,*] [iD] JIANMING DAI,[2] BORIS BRAVERMAN,[3] [iD] XI-CHENG ZHANG,[1] AND ROBERT W. BOYD[1,3] [iD]

[1]*The Institute of Optics, University of Rochester, Rochester, New York 14627, USA*
[2]*Center for Terahertz Waves and School of Precision Instruments & Opto-Electronics Engineering, Tianjin University, Tianjin 300072, China*
[3]*Department of Physics, University of Ottawa, Ottawa K1N 6N5, Canada*
Corresponding author: jzhao24@ur.rochester.edu

In contrast to imaging using position-resolving cameras, single-pixel imaging uses a bucket detector along with spatially structured illumination to compressively recover images. This emerging imaging technique is a promising candidate for a broad range of applications due to the high signal-to-noise ratio (SNR) and sensitivity, and applicability in a wide range of frequency bands. Here, inspired by single-pixel imaging in the spatial domain, we demonstrate a time-domain single-pixel imaging (TSPI) system that covers frequency bands including both terahertz (THz) and near-infrared (NIR) regions. By implementing a programmable temporal fan-out gate based on a digital micromirror device, we can deterministically prepare temporally structured pulses with a temporal sampling size down to 16.00 ± 0.01 fs. By inheriting the advantages of detection efficiency and sensitivity from spatial single-pixel imaging, TSPI enables the recovery of a 5 fJ THz pulse and two NIR pulses with over 97% fidelity via compressive sensing. We demonstrate that the TSPI is robust against temporal distortions in the probe pulse train as well. As a direct application, we apply TSPI to machine-learning-aided THz spectroscopy and demonstrate a high sample identification accuracy (97.5%) even under low SNRs (SNR ~ 10). © 2021 Optical Society of America under the terms of the

1. INTRODUCTION

In the past decade, single-pixel imaging has emerged as a promising technique for frequency bands where high-resolution pixelated sensors are unavailable or impractical [1–3]. Single-pixel imaging uses structured illumination, a bucket detector without spatial resolution, as well as computational algorithms to recover images, which is distinctive from raster-scanning-based imaging, i.e., raster scanning the transverse position of the electromagnetic wave using a bucket detector. Since multiple transverse positions are sampled in each measurement and all electromagnetic waves that have sampled the object are collected by just one single-pixel detector, a higher detection efficiency along with a lower dark count can be expected compared to imaging techniques using raster scanning or cameras, which further leads to an improved sensitivity [1–3]. The image acquisition time in raster-scanning-based imaging scales proportionately with the number of pixels, while single-pixel imaging can efficiently sample the signal in the data acquisition process by using a computational algorithm: compressive sensing (CS) [4]. CS exploits the sparsity of real-world signals by under-sampling these signals, with a number of acquired measurements smaller than the Nyquist-limited number of samples at the same resolution [4]. Thus, CS provides the possibility of fundamentally improving measurement efficiency and lowering the memory requirements for both data storage and transfer.

Imaging a temporal object can be similarly accomplished through the use of a time-resolving detector. To temporally resolve the object, the detector should have a high bandwidth to provide a sufficient sampling rate, which is the temporal analog to the spatial resolution of a sensor array. Nevertheless, due to the limited bandwidth of electronics (usually less than 100 GHz level), imaging ultrafast signals with sub-ps-level oscillation is challenging. Numerous methods including raster scanning [5], spatiotemporal mapping on a camera [6], frequency resolved measurements [7,8], spectro-temporal conversion [9], the use of time lenses [10–17], and temporal ghost imaging [18–25] have been developed to bypass the limited bandwidth of electronics. Even though these methods are widely adopted in many applications, most of them can work only for selected frequency bands. For frequency bands where the devices have not been well developed, such as in the terahertz (THz) band, the choices of ultrafast sensing are limited compared to optical and NIR signals. The most commonly adopted THz sensing method is THz time-domain spectroscopy (TDS), which works as a Fourier-transform spectrometer in the THz band and relies on raster scanning [5]. Even though single-shot THz sensing has been under development for years, it remains technically challenging to measure weak pulses below pJ level due to the limited sensitivity and dynamic range of currently available cameras [6,26–31]. Asynchronous optical sampling has been demonstrated to be effective for real-time THz
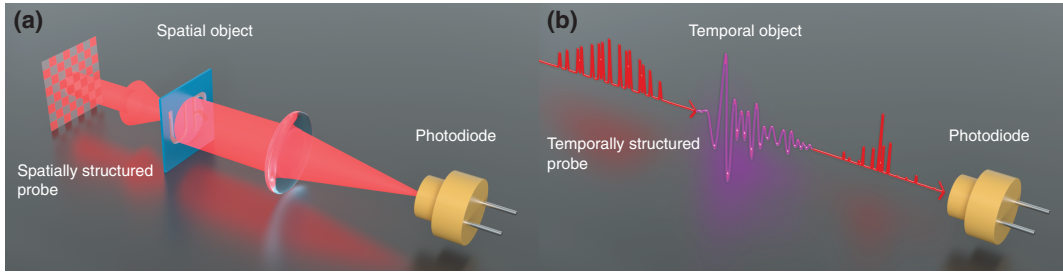
Fig. 1. Comparison of single-pixel imaging and time-domain single-pixel imaging. (a) Typical single-pixel imaging configuration. The photodiode is the bucket detector, which has only one pixel and hence provides no spatial resolution. (b) Our proposed single-pixel temporal imaging configuration. Analogously, the slow photodiode, which lacks the temporal bandwidth to resolve ultrafast signals by itself, works as the "single-pixel" detector in the time domain.

pulse measurement as well [32,33]. Unfortunately, the system has to include two mode-locked ultrafast lasers with a fixed repetition frequency offset. Other techniques, for example, time lenses, frequency resolved optical gating, and spectral phase interferometry for direct electric-field reconstruction, have not yet been developed for the THz frequency band, and the current state of the art of temporal ghost imaging techniques can measure only signals with ps-level oscillation, which is not accurate enough for ultrafast measurements.

Many techniques originally investigated in the spatial domain can inspire the development of analogous techniques in the temporal degree of freedom. The limitations in ultrafast sensing, as discussed earlier, can be resolved by using a time-domain single-pixel imaging (TSPI) system, shown in Fig. 1(b). As the temporal analog of single-pixel imaging, TSPI does not place any requirements on detector bandwidth. That is to say, ultrafast electromagnetic waves can be successfully measured without any mechanical scanning using slow detectors, which are "single-pixel" detectors in the time domain working at corresponding frequency bands. Furthermore, TSPI inherits other advantages of spatial single-pixel imaging: increased sampling efficiency, flexibility for diverse wavelengths and high sensitivity for weak signals. Although TSPI can link ultrafast optical signals with slow electronics, previous demonstrations did not achieve sub-ps-level ultrafast sensing due to the difficulty of deterministically preparing temporally structured pulses with fs-level modulation [23]. Here, we develop a programmable temporal fan-out (TFO) gate based on a commercially available digital micromirror device (DMD), with a minimum temporal sampling size (the temporal interval between two adjacent TFO replicas) $\Delta\tau = 16.00 \pm 0.01$ fs. As the temporal analog of spatial fan-out, which can duplicate an incoming light pulse into spatially separated replicas [34–37], TFO duplicates the input ultrafast pulse into coherent replicas separated in the time domain, forming an ultrafast pulse train. Since the TFO gate is programmable, an ultrafast pulse train with a variable temporal interval and arbitrary temporal structure can be deterministically prepared. It is worth noting that our convenient temporal device not only allows TSPI to image ultrafast signals, but also provides new possibilities in ultrafast waveform synthesis, as well as atomic and molecular control.

2. EXPERIMENTAL CONFIGURATION

Figure 2(a) schematically illustrates the concept of our TSPI scheme. One THz pulse with about 3 V/cm peak electric field and 5 fJ pulse energy works as the temporal object in the current system.

Our TFO gate is shown in the yellow dashed box, which consists of a DMD (Texas Instruments DLP3000) and a lens (L1). The geometry and layout of the DMD are shown in Fig. 2(b). Before the DMD, there is no time delay in the pulse front of the incident pulse $E_{\text{in}}(x, y, z, \omega_0, t)$, and we can write this ultrafast pulse in the form

$$E_{\text{in}}(x, y, z, \omega_0, t) = A_0(x, y) \exp\left(-\frac{t^2}{\tau_w^2}\right) \exp(i\omega_0 t + i\vec{k}\cdot\vec{r}),$$
(1)

where $A_0(x, y)$ is the transverse amplitude distribution. Here we have assumed that our input ultrafast pulse is propagating in the z direction, and has a Gaussian envelope with a carrier frequency of ω_0 as well as a pulse duration equal to τ_w. Since the input pulse is propagating along z direction, the dot product of wave vector $\vec{k}$ and spatial coordinate $\vec{r}$ will equal just a scalar product kz.

After the DMD, N spatiotemporally separated fan-out replicas are generated. L1 is used to perform a Fourier transform so that, in the Fourier plane, the input ultrafast pulse is converted to a pulse train containing N TFO copies $E_{\text{TFO}}(x, y, z, \omega_0, t)$ at the same transverse position with a temporal interval $\Delta\tau$ [38]:

$$E_{\text{TFO}}(x, y, z, \omega_0, t) = \sum_{j=1}^{N} A_j(x, y) \exp\left(-\frac{(t - j\Delta\tau)^2}{\tau_w^2}\right)$$
$$\times \exp(i\omega_0(t - j\Delta\tau) + i\vec{k}_j\cdot\vec{r}), \quad (2)$$

where $A_j(x, y)$ is the amplitude of the jth replica. Due to the origin of each TFO replica from a different position on DMD, the Fourier transform performed by L1 will cause each TFO replica to have a slightly different wave vector $\vec{k}_j$. Then the dot product of $\vec{k}_j$ and $\vec{r}$ can be written as $k_j x \sin\theta_j + k_j y \sin\theta_j + k_j z \cos\theta_j$, where θ_j is the angle between these two vectors. However, since the maximal θ_j in our case is only 0.01 rad, $k_j z \cos\theta_j$ can be accurately approximated as kz and other transverse components can be ignored. Therefore, we will get the final form of TFO outputs $E_{\text{TFO}}(x, y, z, \omega_0, t)$:

$$E_{\text{TFO}}(x, y, z, \omega_0, t) = \sum_{j=1}^{N} A_j(x, y) \exp\left(-\frac{(t - j\Delta\tau)^2}{\tau_w^2}\right)$$
$$\times \exp(i\omega_0(t - j\Delta\tau) + ikz), \quad (3)$$

which represents a sequence of N pulses with duration τ_w and amplitude $A_j(x, y)$ located at temporal position $j\Delta\tau$. N depends on the number of DMD columns illuminated by the incident
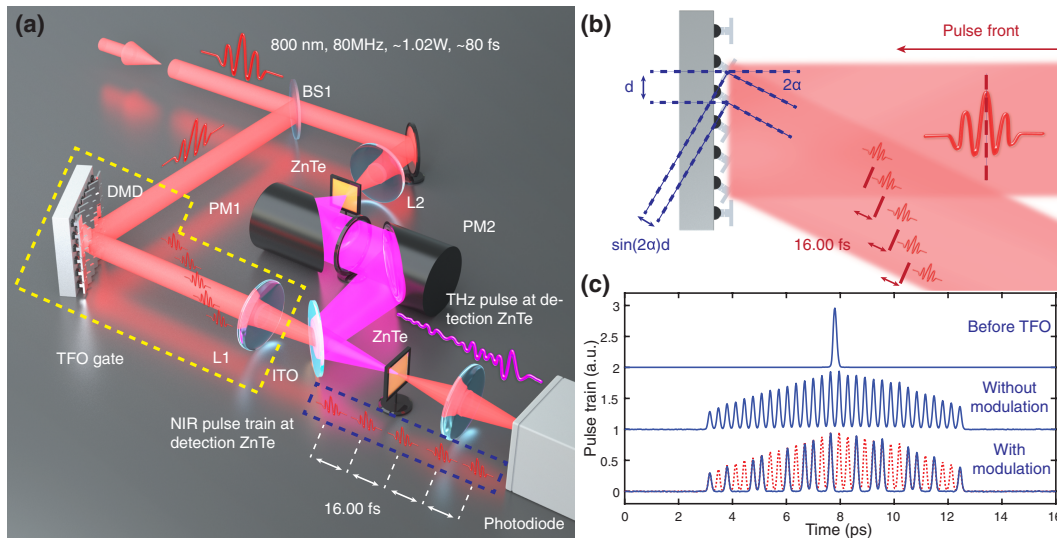
Fig. 2. Schematics of the experimental setup and the structure of the TFO gate. (a) Experimental configuration. The yellow dashed box indicates our TFO gate, and the blue dashed box indicates the prepared ultrafast pulse train at the detection ZnTe crystal plane. (b) A detailed sketch illustrates the layout of the DMD and how its geometry leads to our TFO gate. The dark red arrow shows the propagation direction of input ultrafast pulse. $\alpha = 0.21$ rad is the tilt angle of each micromirror, while $d = 10.8$ µm is the separation between two micromirrors. Dark red lines represent the corresponding pulse front. The $\Delta\tau$ between two TFO copies is given by $\Delta\tau = \sin(2\alpha)d/c = 14.66$ fs, where c is the speed of light in air. Note that, in the experiment, the light is normally incident on the DMD. (c) Examples showing how the TFO works. Each effective TFO replica consists of five DMD columns. Due to the long pulse duration of the NIR pulse, the separation between two effective replicas is 240 fs (15 DMD columns) to explicitly show the structure of pulse trains. The red dashed trace indicates that the TFO copies at those temporal position are turned off by modulating the TFO gate. All cross-correlation traces of pulse trains are averaged over nine measurements.

pulse, which is 608 in the current system. The intensity of each replica can be arbitrarily tuned by enabling only a subset of the mirrors in each DMD column, which further enables arbitrary control over the pulse train (examples are shown in Fig. S2). $\Delta\tau$ is determined by the physical size and tilt angle of the micromirrors. For the current device, the measured $\Delta\tau$ is 16.00 ± 0.01 fs, which is consistent with the theoretical value of 14.66 fs found in the caption of Fig. 2. Therefore, the upper bound of the Nyquist frequency of our TSPI is 31.25 THz, which is sufficient for measuring most broadband pulses. It is worth noting that even though the temporal sampling size can be down to 16.00 ± 0.01 fs, the temporal resolution of TSPI is still fundamentally limited by input pulse duration, which is 80 fs in our experiment. A larger $\Delta\tau$ and a longer pulse duration of each TFO replica can be achieved by combining multiple DMD columns into a single "effective column" due to the interference between adjacent TFO replicas. The total time window T (temporal field of view) depends on the overall size of the mirror array, and is equal to $N \times \Delta\tau$, which is 9.73 ps. TFO replicas interact with the THz pulse in the detection ZnTe crystal. The measurement of THz pulse is achieved based on electro-optic sampling [5]. The polarization state of each TFO replica is modulated by the electric field of the THz pulse at the corresponding temporal position, and the change in polarization is then analyzed using a quarter-wave plate, a Wollaston prism, and a balanced photodiode detector, which are not depicted in Fig. 2.

3. COMPRESSIVE SENSING IN ULTRAFAST MEASUREMENTS

Before we briefly introduce the concept of CS, a computational algorithm for accurate reconstruction of sparse signals, it is convenient to revisit the measurement process in conventional

ultrafast sensing. If we assume that our pulse $E(t)$ is temporally sampled at M time points, the analog signal $E(t)$ will be represented by an M dimensional, digitized vector $E_d(t) = [E(t_1), E(t_2), \ldots, E(t_M)]$. This M dimensional vector $E_d(t)$ is sampled by a sampling matrix S, which is the M dimensional identity matrix in the case of traditional ultrafast sensing techniques based on either raster scanning or high-bandwidth detectors. This identity sampling matrix corresponds to the "natural basis," where the ith sampling row vector represents the sampling at temporal position t_i, and the sampling is experimentally accomplished by using a high-bandwidth detector to measure the pulse at t_i, or raster scanning a slow detector to measure the pulse at t_i. Mathematically, the measurement process can be represented by $\phi = SE_d(t)$, where ϕ is the coefficient vector corresponding to the data recorded by the detector in the experiment. Thus, recovering the digitized pulse $E_d(t)$ based on experimental data ϕ and sampling matrix S is simply given by $E_d(t) = S^{-1}\phi$. Since the sampling basis S is the identity matrix in conventional ultrafast sensing, the experimental measurement result ϕ directly represents the digitized pulse $E_d(t)$.

From the discussion above, it is obvious that at least M measurements, which is the minimal number of measurements required by Nyquist sampling limit, are required to recover the signal because the sampling matrix S has to be inverted. However, by adopting CS, we can significantly reduce the number of measurements to a number smaller than M. Since most signals in nature are sparse when represented in an appropriate basis [4], CS can take advantage of this sparsity and find the proper sparse basis R so that most coefficients in $RE_d(t)$ are close to zero [4]. Therefore, one can recover most information of the signal vector $E_d(t)$ by measuring only those nonzero coefficients in $RE_d(t)$. This indicates that in the experiment, we need to use only sampling vectors whose corresponding coefficients are nonzero to sample the unknown

ultrafast signal. Hence, a number of measurements that is less than M is sufficient to recover the signal without losing too much information, which surpasses the Nyquist sampling limit because of this under-sampling measurement procedure [4].

To fulfill the condition of CS, R has to be incoherent to basis S, which means that the correlation between any two elements in R and S has to be small. Luckily, if R is the Fourier conjugate basis of S, they are always maximally incoherent to each other (a detailed discussion of incoherent basis and choice of sampling basis can be found in Supplement 1 Section 2) [4]. Furthermore, the majority of information in THz signals is carried by low-frequency terms. Based on these two facts, if we use S as the natural basis representing the sampling of temporal position, we will use the Walsh-ordered Hadamard matrix as the sparse sampling basis R in our experiment. This is because the Walsh-ordered Hadamard transform is a generalized discrete Fourier transform, and hence the row vectors of the Walsh-ordered Hadamard matrix represent different frequencies in an increasing order. Therefore, we can either sequentially use each row of the Walsh-ordered Hadamard matrix to sample the ultrafast signal from the low-frequency to high-frequency components, or selectively measure one or more arbitrary frequencies by choosing the corresponding row vectors to encode the probe pulse train. Here, we mainly show the result of sequential sampling.

The procedure of the sampling and data processing is shown in Fig. 3(b). We first use each row vector of the 128-dimensional Walsh-ordered Hadamard matrix [shown in Fig. 3(a)] to modulate the pulse train via the TFO gate. The encoded pulse train is then used to sample the temporal object, which is a 5 fJ THz pulse. After the interaction between two pulses, the signal is recorded by a slow photodiode, which works as the "single-pixel" detector in the time domain. By correlating the rows of the sampling matrix and corresponding signal recorded on the detector, we can recover the temporal object.

4. EXPERIMENTAL RESULTS

Figure 4 shows the THz pulses reconstructed based on TSPI and the flow chart in Fig. 3. The quantity describing the level of compression is termed as compression ratio (CR), which is defined

as the ratio between the number of measurements taken in the experiment over M, i.e., measuring all the rows of the Hadamard matrix. Limited by the pulse duration of the original pulse (80 fs), we choose $\Delta\tau$ to be 64 fs by combining four DMD columns into one effective column. One-hundred-twenty-eight TFO replicas, encoded by the 128-dimensional Walsh-ordered Hadamard matrix, constitute our probing pulse train with $T = 8.19$ ps. The red curves are THz fields and spectra measured by raster scanning a mechanical delay stage without averaging. To quantitatively compare the signal recovered by TSPI and the ground truth, we introduce fidelity as the cross-correlation coefficient between two state vectors. If we define the state of the THz fields measured by raster scanning as $|E_{\mathrm{RS}}\rangle$, and define the THz fields recovered by CS as $|E_{\mathrm{CS}}\rangle$, we define the fidelity F with the following expression:

$$F = \frac{\langle E_{\mathrm{CS}}|E_{\mathrm{RS}}\rangle}{\sqrt{\langle E_{\mathrm{CS}}|E_{\mathrm{CS}}\rangle\langle E_{\mathrm{RS}}|E_{\mathrm{RS}}\rangle}}. \tag{4}$$

As illustrated in Fig. 4(d), by sacrificing high-frequency components, a recovered THz pulse with high fidelity (84.30%) can be achieved even at 20% CR. At this CR of 20%, the last sampling pulse train is encoded by the 25th row of the Walsh-ordered Hadamard matrix, which results in the cutoff sampling frequency at 1.5 THz and a weak sidelobe at 2.4 THz. For a CR of 30%, additional high-frequency terms are measured, and in the spectrum, almost all high-frequency terms in THz pulse are collected, leading to a near-unity fidelity of 97.43% in THz field. As the CR goes higher to 40%, more high-frequency components are collected, but the improvement is limited (fidelity of 97.76% in field). When we look at the spectrum, two spectra match well for all frequencies except for some noise, which indicates that we have included enough high frequencies in the measurement. Therefore, all higher-frequency terms can be ignored due to their relatively small contributions.

Compared to the data acquisition time of the mechanical stage raster scanning data (sampling rate at 2 Hz, which is mainly limited by the stability of our mechanical stage, leading to a measurement time of ∼64 s), our TSPI system requires only ∼15 s with 30% CR (sampling rate at 10 Hz). The data acquisition time can be improved to be less than 4 s by using a laser pulse with a shorter pulse duration (see Supplement 1 Sections 1 and 5), and can be
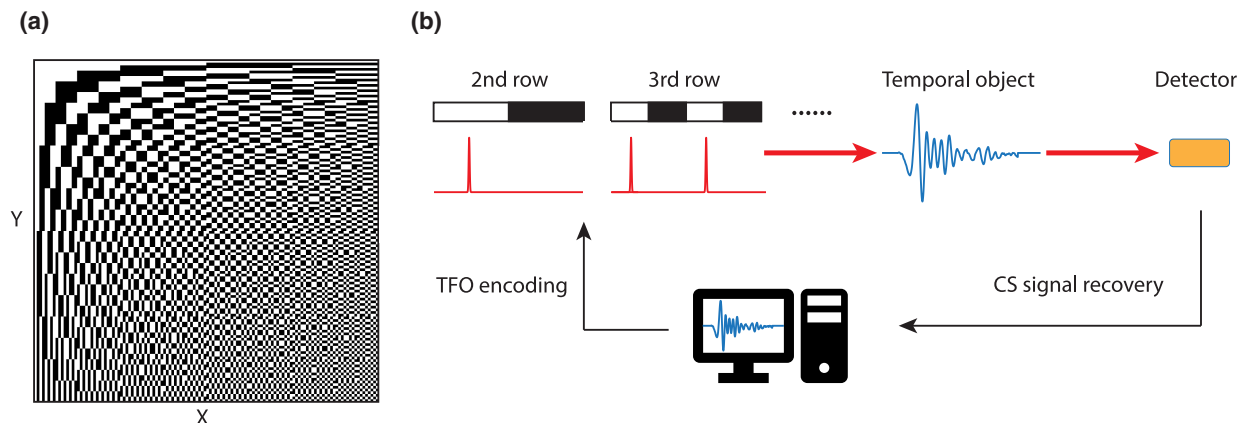

Fig. 3. Walsh-ordered Hadamard matrix and the flow chart of the sampling and data processing based on CS. (a) 128-dimensional Walsh-ordered Hadamard matrix, which is used to sample the temporal object in our experiment. (b) Flow chart of the experiment. The probe pulse is temporally modulated by the TFO gate, which is controlled by the computer, based on the row vectors of the Walsh-ordered Hadamard matrix. By correlating the row vectors and the corresponding signals registered on the detector, we can recover the temporal object on the computer. Note that all the arrows shown are used to guide the viewer through the sampling and signal recovery process, but not indicate the propagation direction of light pulse.
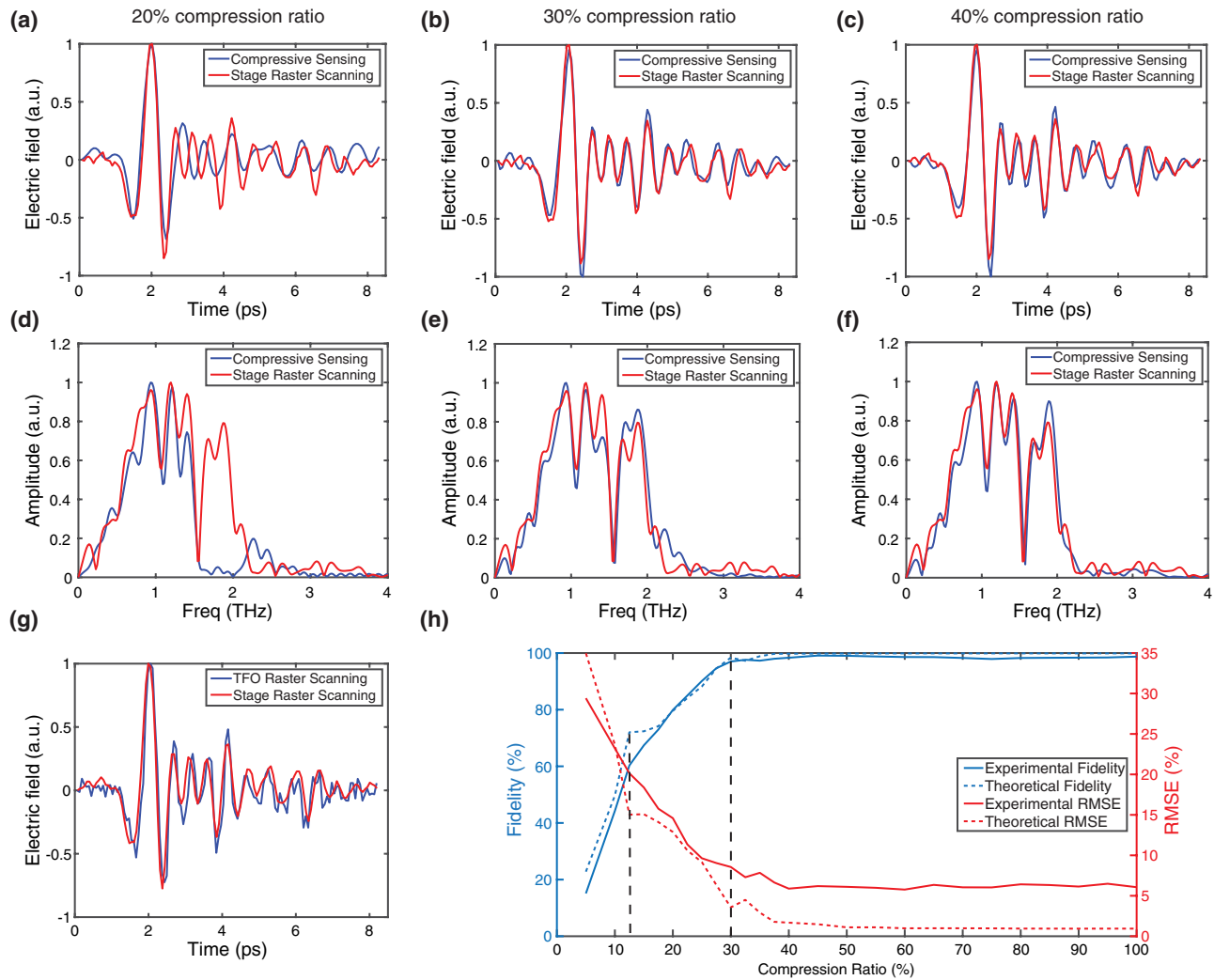
Fig. 4. Recovered THz electric fields and spectra at different CRs (blue curves). The THz fields and spectra measured by raster scanning a mechanical delay stage (red curves) are shown for comparison. (a), (d) Recovered THz field and spectrum at 20% CR. The fidelity in THz field is 84.30%. and the root mean square error (RMSE) is 14.92%. (b), (e) Recovered THz field and spectrum at 30% CR. The fidelity in THz field is 97.43%, and the RMSE is 7.69%. (c), (f) Recovered THz field and spectrum at 40% CR. The fidelity in THz field is 97.76%, and the RMSE is 7.17%. THz pulses recovered by both CS and raster scanning are measured without averaging and use the same $\Delta\tau$ (64 fs). Due to the limited detection bandwidth of ZnTe crystal, we show the spectra only in 0–4 THz range. (g) Raster scanning using the TFO gate. The sampling rate and acquisition time of each measurement are set to be the same as CS data. Fidelity is 87.35% and RMSE is 13.11%. (h) Measured and theoretical fidelities and RMSEs as functions of CR. The RMSE is mainly limited by the measurement noise.

further reduced below 1 s by upgrading the experimental hardware (see Supplement 1 Section 7). Due to the fewer measurements enabled by CS and the faster sampling speed provided by the DMD, TSPI can reduce data acquisition time, data storage, and transfer memory requirements by a factor of at least 2/3, which would significantly enhance system efficiency in this era of big data. It is also worth noting that the data processing time is less than ∼0.7 s for a 30% CR result using MATLAB on a normal laptop. The processing time for CS will become shorter with better sparsity, smaller number of iterations, and more efficient optimization strategy. For example, we use a total variation regularization with L2 norm (TV/L2) model for denoising with 15 iterations to compressivly recover the THz signal [39]. Apart from executing the MATLAB code on a more powerful machine, a shorter processing time can be available when the efficient TV model is used with fewer iterations. Apart from a more efficient measurement, CS is also more robust to noise than raster scanning because of the denoising in the optimization strategy. As shown in Fig. 4(g), under

the same sampling rate and integration time of each measurement, the fidelity of the TFO raster scanning data, i.e., sequentially turning on each DMD column, is only 87.35% and the RMSE is 13.11%, which are worse than the CS data even when the CR is only 30%. Even though the data acquisition time of the TFO raster scanning data is 13 s, the TSPI scheme is still better than the raster scanning method due to the use of CS, leading to the inherent advantage of robustness against noise, and a potentially even shorter data acquisition time with a shorter pulse duration laser pulse. It is worth noting that, even without using CS and TSPI, our TFO gate can also provide a much faster raster scanning rate (up to 4 kHz for the current device) than conventional mechanical stages (10 Hz for the current device).

The experimental results of the fidelity and RMSE as a function of CR, shown in Fig. 4(h), are in good agreement with our theoretical predictions, which is shown in Supplement 1 Fig. S1. As the CR increases, both fidelity and RMSE change dramatically at first, and then gradually level out after the CR reaches 30%.
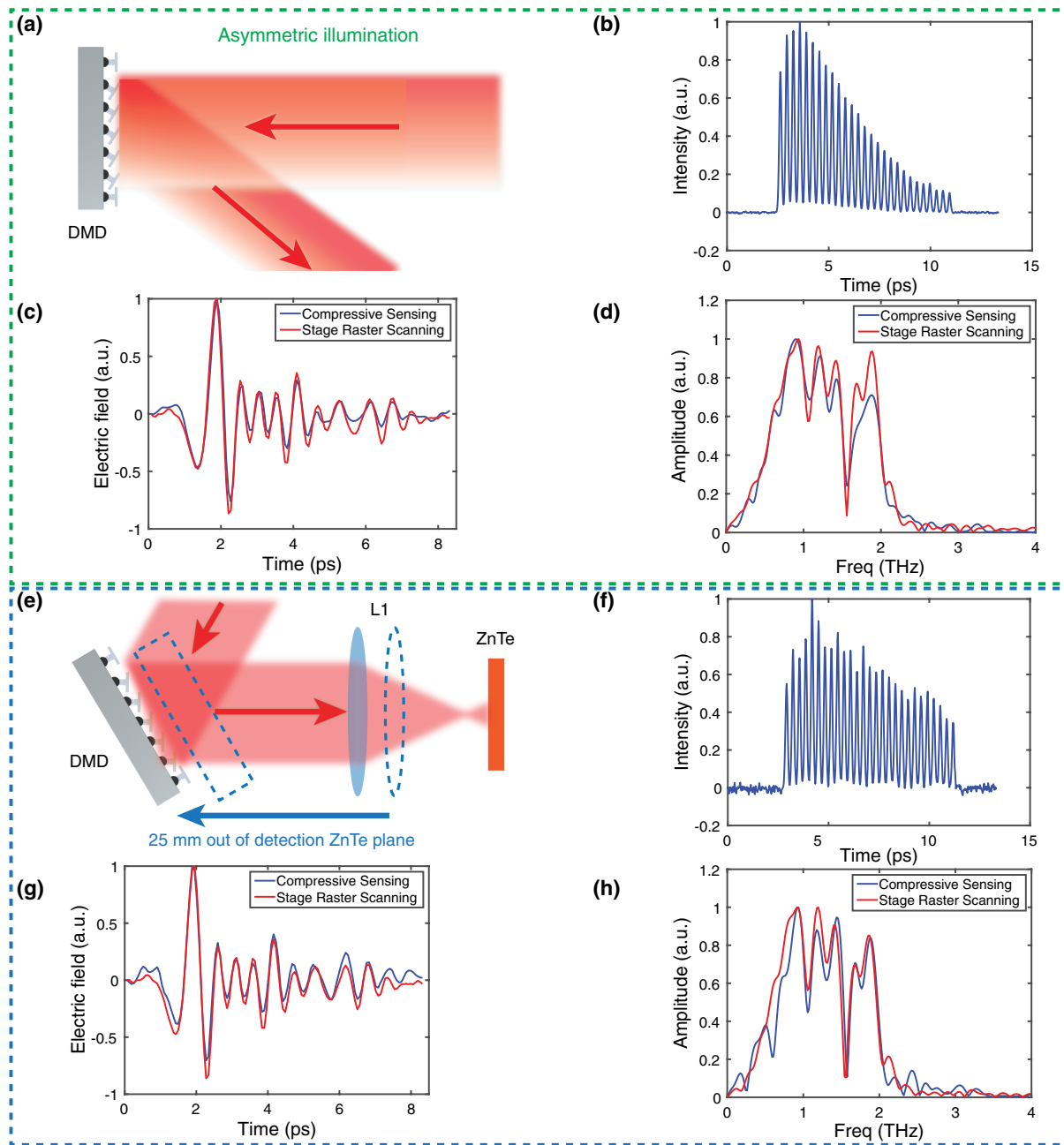
Fig. 5.   Recovered THz electric fields and spectra using the distorted TFO gate at 40% CR. Red arrows illustrate the propagation direction of NIR pulses. (a) How we distort the TFO gate with an asymmetric illumination. (b) Measured asymmetric pulse train formed by the distorted TFO copies. The ratio between the maximal and minimal intensities in (b) is about 10. As a comparison, this ratio is about three in Fig. 2(c), while the SNR is the same ($\sim$350). (c), (d) Corresponding recovered THz field and spectrum. The RMSE in field is 7.21%. (e) How we move the Fourier plane of the DMD 25 mm away from the detection ZnTe plane by moving the TFO gate in the direction as the blue arrow shows. (f) Measured pulse train when the detection ZnTe crystal is 25 mm out of the Fourier plane of the DMD. The intensity envelope becomes irregular and SNR is poor ($\sim$80). (g), (h) Recovered THz pulse and spectrum using the distorted pulse train in (f). The RMSE in field is 7.66%. (b), (f) Averaged results of nine measurements, while THz pulses recovered by CS and raster scanning have no averaging. All results shown are consistent with theoretical predictions in Supplement 1 Section 5.

Our theoretical model also predicts that there are two discontinuity points in the slope of both RMSE and fidelity curves. As indicated by the two vertical dashed lines, the first turning point is located at CR equal to 12.5%, while the second one is at CR equal to 30%. The slopes in both RMSE and fidelity curves abruptly decrease to a slower rate and can even change sign after the turning points. Our speculation of the underlying physics behind these turning points can be found in Supplement 1 Section 2. Similar

observations have been found in spatial single-pixel imaging work when the sampling matrix is reordered [40]. Therefore, in both spatial and temporal CS, one can optimize the acquired information within a given CR by rearranging the sampling order, which demonstrates the spatiotemporal duality of light pulses. An improved measurement efficiency can be predicted by further optimizing the sampling strategy based on these turning points.

5. ROBUSTNESS AGAINST TEMPORAL DISTORTIONS

Similar to its spatial counterpart, TSPI is resistant to temporal distortions. To demonstrate this robustness, we first intentionally make the illumination on the DMD asymmetric, which is shown in Fig. 5(a). This results in a different intensity for each TFO replica, and further leads to asymmetric pulse trains in the time domain [Fig. 5(b)]. Despite the distorted TFO replicas, the recovered THz signal, shown in Figs. 5(c) and 5(d), has a fidelity of 96.96% in the field at 40% CR. The major information loss comes from underestimation of oscillations at the tail of the THz pulse (above 5 ps), which results from the weak intensities of TFO replicas at the end of the pulse train. Next, as illustrated by the blue arrow in Fig. 5(e), we move the location of the Fourier plane of the DMD 25 mm away from the ZnTe crystal by moving the TFO gate. Due to the spread of k-vectors of each replica at the Fourier plane, the TFO copies will be spatiotemporally separated at the detection crystal plane. This leads to the spatiotemporal coupled sampling, which yields an irregular pulse train envelope and lowers the intensity of each sub-pulse [Fig. 5(f)]. Nevertheless, as shown in Figs. 5(g) and 5(h), distorted pulse trains do not affect the quality of the recovered signal, which has a fidelity of 98.34% in field at 40% CR. Such a robustness comes from the fact that this amplitude distortion leads only to the over- and under-estimation of the amplitude distribution of the object. Therefore, the temporal structure, and hence the spectral structure, of the sampling pulse train is not impacted. In our measurement, we are taking advantage of the spectral sparsity of the signal. Therefore, as long as the distorted sampling pulse trains are measuring the desired information carried by low-frequency terms, CS can provide an accurate recovery of the original object.

6. RECOVERY OF NIR PULSES WITH DIFFERENT PULSE DURATIONS

To demonstrate that TSPI can work for signals in a broad range of frequencies, we recover two 800 nm NIR pulses with ~90 fs and ~125 fs pulse durations. To perform the measurement, the detection crystal is changed to a 1 mm thick BBO crystal, and sum-frequency generation is employed. A photomultiplier tube is used as the new detector to replace the balanced photodiodes in THz measurements. Due to the long pulse duration of our laser (80 fs), preparing high-contrast sampling pulse trains with 16 fs temporal modulation size is not feasible. Therefore, we have to implement a rolling-average strategy to measure NIR pulses with 16 fs sampling size. To do this, we first combine five DMD columns together (80.00 fs) as an effective column. Then we perform the measurement of the unknown pulse in one time window. Next, we shift this time window 16.00 fs forward to make another set of measurements, which corresponds to the shift of one DMD column. We continue this rolling process until five shifts are done. The final recovered NIR pulse is the rolling average of the measurements of all five shifts.

The experimental results are shown in Fig. 6. We change the pulse duration in the signal arm by pre-chirping the laser pulse using the self-phase modulation effect inside a ZnTe crystal (the crystal in the signal arm). In the meantime, the pulse duration of the probe arm is kept at 80 fs. Figure 6(a) is the compressive
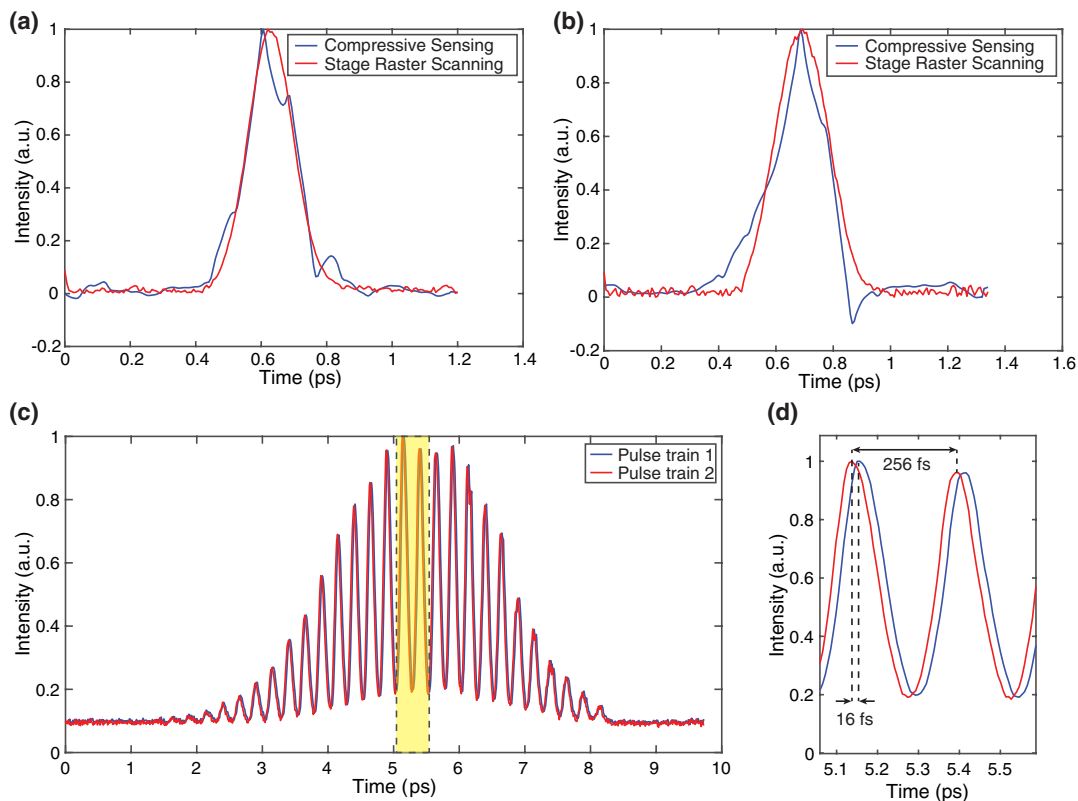

Fig. 6. Recovered NIR pulses (blue curves) and measured results using raster scanning (red curves). (a) Recovered NIR pulse with 90 fs pulse duration at 80% CR. (b) Recovered NIR pulse with 125 fs pulse duration at 80% CR. (c) Two pulse trains used for NIR measurement. By shifting one DMD column, we shift pulse train 1 16 fs forward to get pulse train 2. (d) Details of the measured pulse trains shown in the black dashed box in (c). One can find that the displacement between two pulse trains is 16 fs, while the separation between two peaks in one pulse train is 256 fs.

measurement result (blue curve) of a 90 fs pulse compared to the delay stage result (red curve). The recovered signal has a fidelity of 98.48% in pulse shape, while the pulse duration is 91.4 fs. Figure 6(b) shows the compressive result of a 125 fs pulse. The fidelity is 97.88%, while the pulse duration is 110.0 fs. Both CS results are measured at 80% CR due to the fact that NIR pulses carry more high-frequency components. The main limiting factor in NIR pulse measurement is the instability of the signal pulse induced by self-phase modulation. This instability not only leads to a worse SNR (less than 70 in delay stage data), but also results in irregular but large intensity fluctuations at the peak. When these significant sources of noise are included in CS recovery, we will have a distorted pulse. For example, in the imperfect reconstruction of the 125 fs pulse, we have observed a negative sidelobe at 0.85 ps in Fig. 6(b), which has no physical meaning because the measured quantity is the pulse intensity. This phenomenon also happens in the single-pixel imaging system and can be mitigated using additional data processing algorithms. Therefore, a better recovery should be available with additional data processing algorithms, and for real NIR pulses whose pulse durations are not extended by nonlinear effects. To get a more accurate CS recovery, one can also intentionally stretch the NIR pulses, for example, using time lenses, to a longer level and then use our TSPI to measure it [10–17]. It is notable that the TSPI system can be used for other wavelengths as well. One simply needs to replace the crystal and detector with the ones at the correct frequency band.

7. MACHINE-LEARNING-AIDED THz SPECTROSCOPY

Last, we demonstrate a compressive ultrafast THz TDS system as one potential application of TSPI, and show that we can improve its performance through use of machine learning (ML). Five different samples (water vapor, glucose, lactose, benzoic acid, and $KCLO_4$) are tested in the system, and 1000 sets of data of each sample are used for training. To show the noise resistance of the ML-enhanced TDS system, the SNR of the THz pulse is decreased to $\sim$10 by attenuating the THz pulse to sub-fJ level and lowering the integration time on the lock-in amplifier. As shown in Fig. 7(a), without the help of ML, the measured THz spectra are noisy, and by calculating the maximum fidelity to the reference waveforms, the classification accuracy is only 34.2%. As a comparison, after training our convolutional neural network (CNN) with 5000 sets of data, we can successfully classify the remaining 2000 sets of data (400 for each sample) with an accuracy of 97.50% at 40% CR (see Supplement 1 Section 6 for confusion matrices). If one further reduces the SNR by increasing the sampling rate from 20 Hz to 50 Hz, the identification accuracy will significantly decrease as shown in Fig. 7(b). Therefore, if training data sets are measured using other approaches with worse robustness against noise, for instance, raster scanning, a high identification accuracy will not be achieved even with the help of ML.

8. DISCUSSION AND CONCLUSION

As one can notice, the performance of the TSPI system relies on the temporal interval between two sampling replicas $\Delta\tau$, the number of sampling replicas N, and the total time window T. Luckily, by selecting a DMD chip with the appropriate specifications, different $\Delta\tau$, N, and T can be achieved. The encoding speed is mainly limited by the switching speed of the DMD, which can be as large as 4 kHz in our system and can be further increased to 20 kHz by using a faster DMD chip [41]. One of the beauties of TSPI is that the temporal sampling size comes from modulation on
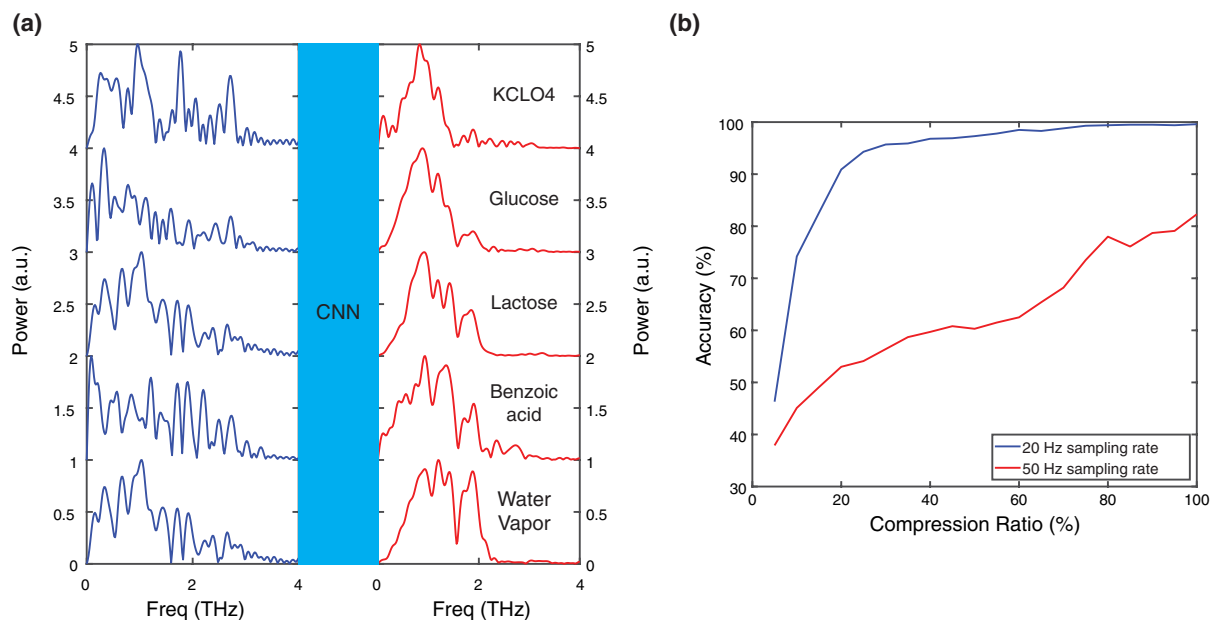

Fig. 7. CNN-enhanced THz spectroscopy. (a) The sample classification is based on a CNN. Due to the poor SNR, the fingerprints of each sample are lost and cannot be identified from spectra (blue curves), which leads to a classification accuracy of 34.2% without the use of ML. Red curves are desired spectra that we are trying to match. After training the CNN, we have an average classification accuracy of 96.8% at 40% CR. (b) Accuracy as a function of CR. When the sampling rate is 20 Hz, the accuracy rises quickly when the CR increases from 5% to 20%, and then starts to converge, which has a very similar behavior as the fidelity shown in Fig. 4(h). As a comparison, when sampling rate is 50 Hz, the SNR in each measurement becomes 1.73 times smaller than the 20 Hz sampling rate case, and accuracy curve does not start converging even when CR is 100%. All identification accuracies are averaged over five CNN trainings.

the TFO gate but not from the bandwidth of detectors. Therefore, our scheme solely requires detectors with bandwidth exceeding the modulation frequency of the DMD, allowing the use of kHz-level photodiodes, which have better noise-equivalent power than GHz-level fast photodiodes. As a comparison, previous temporal imaging schemes, including the use of time lenses and temporal ghost imaging, cannot easily reach such high effective sampling rate and sensitivity even with the use of fast detectors with bandwidths at 100 GHz level [10–25]. Due to encoding the probe beam as opposed to temporally modulating the THz pulses [42], our simple and reliable scheme can directly utilize commercially available DMDs with a high modulation speed and damage threshold, and hence no additional fabrication of devices is required.

Raster scanning the time delay between a short probe pulse and the signal pulse is the conventional approach for ultrafast sensing. As a contrast, TSPI can significantly reduce the data acquisition time in the sampling process, and provide a better fidelity as well as enhanced robustness against noise [comparison in Fig. 4(g)], although this can come at a cost of a reduced temporal field of view. It is worth noting that a larger temporal field of view can be achieved not only by implementing an advanced DMD, but also through a suitably synchronized combination of DMD and mechanical stage.

Compared to methods using cameras or spectrometers, TSPI is applicable to both weak and strong pulses at various frequency bands. Even though cameras and spectrometers enable the possibility of single-shot measurements, effective measurement of weak pulses is not applicable at some wave bands. For example, in the THz region, these single-shot measurement methods usually require the use of μJ-to-mJ-level pump pulses to generate pJ-to-nJ-level THz pulses [6,26–31]. As a comparison, our approach needs only nJ-level pump pulses, and is capable of measuring fJ-level THz pulses. Hence, the sensitivity of our system is about three orders of magnitude better than camera- or spectrometer-based methods. Furthermore, when pulses become weak, these single-shot measurement methods will need to average over multiple shots to provide a good SNR, which is no longer a single-shot measurement and will result in a slow measurement speed as well. However, for NIR and optical pulse measurements, our method does not presently resolve spectral phase, and minimal resolvable pulse duration cannot be below 10 fs. Therefore, even though our approach is applicable for weak THz pulses, the current demonstration cannot provide comprehensive characterization of NIR and optical pulses compared to frequency-resolved optical gating and spectral phase interferometry for direct electric-field reconstruction [7,8]. The possible spectral phase measurement might be available by introducing another phase-only spatial light modulator (SLM) to the probe arm to include phase encoding.

Temporal imaging based on time lenses is another way to measure ultrafast signals. By stretching the pulse to a longer duration, one can use fast photodiodes to measure optical pulses [10–17]. Even though the ultrafast measurement performed using time lenses can be single-shot and provide a better temporal field of view, our technique is still advantageous in terms of the simplicity, working frequency bands, and flexibility. All components in TSPI are commercially available without requiring additional design or fabrication. The working frequency bands of time lenses is usually at optical and NIR regions, and time lenses in the THz band have not been demonstrated yet. Meanwhile, even in the optical and NIR wave bands, the design and fabrication of photonic time lenses

have to be changed for each wavelength due to the specifically designed dispersion compensation mentioned in Refs. [13–17]. As a comparison, our TSPI requires solely the nonlinear interaction between probe pulse and signal pulse, and can be used anytime that a conventional electro-optic (EO) sampling measurement with a delay stage could be used.

It is worth noting that a spatiotemporal characterization of ultrafast pulse can be available by combining TSPI and our previous spatial sampling system, which might lead to a concise THz single-pixel hyperspectral imaging system [42]. Since both approaches are based on probe-beam encoding, one can use multiple DMDs in the probe arm to deterministically encode spatial and temporal structures onto the NIR probe beam. By implementing CS and such a spatiotemporally structured probe beam, it is possible to comprehensively and compressively measure the THz pulse with high measurement efficiency, which can significantly reduce the data acquisition time and data storage requirement in conventional hyperspectral imaging systems.

In summary, based on an ultrafast TFO gate, we develop a TSPI system to compressively measure ultrafast signals using exclusively kHz-rate slow detectors. The 16.00 ± 0.01 fs temporal sampling size enables the successful measurement of a 5 fJ THz pulse and two NIR pulses with high fidelity. The robustness of TSPI against temporal distortion is also demonstrated. Last, we show that our technique can be used to perform ultrafast THz TDS with the help of ML. Our TSPI system can cover a frequency band including both NIR and THz regions with high sensitivity, efficiency, and robustness. This distinctive technique can provide dynamic temporal imaging of ultrafast signals, leading to potential applications including single-pixel hyperspectral imaging, remote sensing, and high-data-rate optical communications.

Disclosures. The authors declare no conflicts of interest.

Data availability. Data underlying the results presented in this paper are not publicly available at this time but may be obtained from the authors upon reasonable request.

Supplemental document. See Supplement 1 for supporting content.

REFERENCES

1. Y. Altmann, S. McLaughlin, M. J. Padgett, V. K. Goyal, A. O. Hero, and D. Faccio, "Quantum-inspired computational imaging," Science **361**, eaat2298 (2018).
2. M. P. Edgar, G. M. Gibson, and M. J. Padgett, "Principles and prospects for single-pixel imaging," Nat. Photonics **13**, 13–20 (2019).
3. G. M. Gibson, S. D. Johnson, and M. J. Padgett, "Single-pixel imaging 12 years on: a review," Opt. Express **28**, 28190–28208 (2020).
4. E. J. Candès and M. B. Wakin, "An introduction to compressive sampling," IEEE Signal Processing Magazine **25**(2), 21–30 (2008).
5. Q. Wu and X.-C. Zhang, "Free-space electro-optic sampling of terahertz beams," Appl. Phys. Lett. **67**, 3523–3525 (1995).

6. S. M. Teo, B. K. Ofori-Okai, C. A. Werley, and K. A. Nelson, "Invited article: single-shot THz detection techniques optimized for multi-dimensional thz spectroscopy," Rev. Sci. Instrum. **86**, 051301 (2015).

7. D. J. Kane and R. Trebino, "Characterization of arbitrary femtosecond pulses using frequency-resolved optical gating," IEEE J. Quantum Electron. **29**, 571–579 (1993).

8. C. Iaconis and I. A. Walmsley, "Spectral phase interferometry for direct electric-field reconstruction of ultrashort optical pulses," Opt. Lett. **23**, 792–794 (1998).

9. M. Kauffman, W. Banyai, A. Godil, and D. Bloom, "Time-to-frequency converter for measuring picosecond optical pulses," Appl. Phys. Lett. **64**, 270–272 (1994).

10. B. H. Kolner and M. Nazarathy, "Temporal imaging with a time lens," Opt. Lett. **14**, 630–632 (1989).

11. B. H. Kolner, "Space-time duality and the theory of temporal imaging," IEEE J. Quantum Electron. **30**, 1951–1963 (1994).

12. C. Bennett and B. Kolner, "Upconversion time microscope demonstrating 103 × magnification of femtosecond waveforms," Opt. Lett. **24**, 783–785 (1999).

13. R. Salem, M. A. Foster, A. C. Turner, D. F. Geraghty, M. Lipson, and A. L. Gaeta, "Optical time lens based on four-wave mixing on a silicon chip," Opt. Lett. **33**, 1047–1049 (2008).

14. M. A. Foster, R. Salem, D. F. Geraghty, A. C. Turner-Foster, M. Lipson, and A. L. Gaeta, "Silicon-chip-based ultrafast optical oscilloscope," Nature **456**, 81–84 (2008).

15. M. A. Foster, R. Salem, Y. Okawachi, A. C. Turner-Foster, M. Lipson, and A. L. Gaeta, "Ultrafast waveform compression using a time-domain telescope," Nat. Photonics **3**, 581–585 (2009).

16. Y. Okawachi, R. Salem, A. R. Johnson, K. Saha, J. S. Levy, M. Lipson, and A. L. Gaeta, "Asynchronous single-shot characterization of high-repetition-rate ultrafast waveforms using a time-lens-based temporal magnifier," Opt. Lett. **37**, 4892–4894 (2012).

17. A. Tikan, S. Bielawski, C. Szwaj, S. Randoux, and P. Suret, "Single-shot measurement of phase and amplitude by using a heterodyne time-lens system and ultrafast digital time-holography," Nat. Photonics **12**, 228–234 (2018).

18. T. Shirai, T. Setälä, and A. T. Friberg, "Temporal ghost imaging with classical non-stationary pulsed light," J. Opt. Soc. Am. B **27**, 2549–2555 (2010).

19. P. Ryczkowski, M. Barbier, A. T. Friberg, J. M. Dudley, and G. Genty, "Ghost imaging in the time domain," Nat. Photonics **10**, 167–170 (2016).

20. F. Devaux, P.-A. Moreau, S. Denis, and E. Lantz, "Computational temporal ghost imaging," Optica **3**, 698–701 (2016).

21. Y. O-oka and S. Fukatsu, "Differential ghost imaging in time domain," Appl. Phys. Lett. **111**, 061106 (2017).

22. P. Ryczkowski, M. Barbier, A. T. Friberg, J. M. Dudley, and G. Genty, "Magnified time-domain ghost imaging," APL Photon. **2**, 046102 (2017).

23. Y.-K. Xu, S.-H. Sun, W.-T. Liu, G.-Z. Tang, J.-Y. Liu, and P.-X. Chen, "Detecting fast signals beyond bandwidth of detectors based on computational temporal ghost imaging," Opt. Express **26**, 99–107 (2018).

24. H. Wu, P. Ryczkowski, A. T. Friberg, J. M. Dudley, and G. Genty, "Temporal ghost imaging using wavelength conversion and two-color detection," Optica **6**, 902–906 (2019).

25. Y. Tian, H. Ge, X.-J. Zhang, X.-Y. Xu, M.-H. Lu, Y. Jing, and Y.-F. Chen, "Acoustic ghost imaging in the time domain," Phys. Rev. Appl. **13**, 064044 (2020).

26. Z. Jiang and X.-C. Zhang, "Single-shot spatiotemporal terahertz field imaging," Opt. Lett. **23**, 1114–1116 (1998).

27. J. Shan, A. S. Weling, E. Knoesel, L. Bartels, M. Bonn, A. Nahata, G. A. Reider, and T. F. Heinz, "Single-shot measurement of terahertz electromagnetic pulses by use of electro-optic sampling," Opt. Lett. **25**, 426–428 (2000).

28. K. Kim, B. Yellampalle, G. Rodriguez, R. Averitt, A. Taylor, and J. Glownia, "Single-shot, interferometric, high-resolution, terahertz field diagnostic," Appl. Phys. Lett. **88**, 041123 (2006).

29. K. Kim, B. Yellampalle, A. Taylor, G. Rodriguez, and J. Glownia, "Single-shot terahertz pulse characterization via two-dimensional electro-optic imaging with dual echelons," Opt. Lett. **32**, 1968–1970 (2007).

30. Y. Kawada, T. Yasuda, A. Nakanishi, K. Akiyama, and H. Takahashi, "Single-shot terahertz spectroscopy using pulse-front tilting of an ultra-short probe pulse," Opt. Express **19**, 11228–11235 (2011).

31. S. Zheng, X. Pan, Y. Cai, Q. Lin, Y. Li, S. Xu, J. Li, and D. Fan, "Common-path spectral interferometry for single-shot terahertz electro-optics detection," Opt. Lett. **42**, 4263–4266 (2017).

32. T. Yasui, E. Saneyoshi, and T. Araki, "Asynchronous optical sampling terahertz time-domain spectroscopy for ultrahigh spectral resolution and rapid data acquisition," Appl. Phys. Lett. **87**, 061101 (2005).

33. A. Bartels, R. Cerna, C. Kistner, A. Thoma, F. Hudert, C. Janke, and T. Dekorsy, "Ultrafast time-domain spectroscopy based on high-speed asynchronous optical sampling," Rev. Sci. Instrum. **78**, 035107 (2007).

34. H. Dammann and K. Görtler, "High-efficiency in-line multiple imaging by means of multiple phase holograms," Opt. Commun. **3**, 312–315 (1971).

35. D. Prongué, H.-P. Herzig, R. Dändliker, and M. T. Gale, "Optimized kinoform structures for highly efficient fan-out elements," Appl. Opt. **31**, 5706–5711 (1992).

36. L. A. Romero and F. M. Dickey, "Theory of optimal beam splitting by phase gratings. I. One-dimensional gratings," J. Opt. Soc. Am. A **24**, 2280–2295 (2007).

37. M. Mirhosseini, M. Malik, Z. Shi, and R. W. Boyd, "Efficient separation of the orbital angular momentum eigenstates of light," Nat. Commun. **4**, 2781 (2013).

38. K. Murate, M. J. Roshtkhari, X. Ropagnol, and F. Blanchard, "Adaptive spatiotemporal optical pulse front tilt using a digital micromirror device and its terahertz application," Opt. Lett. **43**, 2090–2093 (2018).

39. C. Li, "Compressive sensing for 3D data processing tasks: applications, models and algorithms," Tech. rep. (2011).

40. M.-J. Sun, L.-T. Meng, M. P. Edgar, M. J. Padgett, and N. Radwell, "A Russian dolls ordering of the Hadamard basis for compressive single-pixel imaging," Sci. Rep. **7**, 3464 (2017).

41. R. I. Stantchev, X. Yu, T. Blu, and E. Pickwell-MacPherson, "Real-time terahertz imaging with a single-pixel detector," Nat. Commun. **11**, 2535 (2020).

42. J. Zhao, E. Yiwen, K. Williams, X.-C. Zhang, and R. W. Boyd, "Spatial sampling of terahertz fields with sub-wavelength accuracy via probe-beam encoding," Light Sci. Appl. **8**, 55 (2019).